Macromolecules **23**, 1139 (1990).
9. J. San Roman, J. Guzman, E. Riande, J. Santoro, M. Rico, *ibid.* **15**, 609 (1982).
10. P. J. Flory and J. E. Mark, *Makromol. Chem.* **75**, 11 (1964); A. Abe, J. W. Kennedy, P. J. Flory, *J. Polym. Sci. Polym. Phys. Ed.* **14**, 1337 (1976); A. Abe and J. E. Mark, *J. Am. Chem. Soc.* **98**, 6468 (1976); A. Abe, K. Tasaki, J. E. Mark, *Polym. J.* **17**, 883 (1985).
11. A. Ajji, J. Guèvremont, K. C. Cole, M. M. Dumoulin, *Polymer* **37**, 3707 (1996).
12. X. Yang, F. Long, D. Shen, R. Qian, *ibid.* **32**, 125 (1991).
13. J. C. Rodriguez-Cabello, L. Quintanilla, J. M. Pastor, *J. Raman Spectrosc.* **25**, 335 (1994).
14. M. Yazdanian, I. M. Ward, H. Brody, *Polymer* **26**, 1779 (1985); A. Cunningham, I. M. Ward, H. A. Willis, V. Zichy, *ibid.* **15**, 749 (1974).
15. S. B. Lin and J. L. Koenig, *J. Polym. Sci. Polym. Phys. Ed.* **20**, 2277 (1982); J. Liu and J. L. Koenig, *Anal. Chem.* **59**, 2609 (1987).
16. R. F. Rapold, U. W. Suter, D. N. Theodorou, *Macromol. Theory Simul.* **3**, 19 (1994).
17. K. Schmidt-Rohr and H. W. Spiess, *Multidimensional Solid-State NMR and Polymers* (Academic Press, London, 1994).
18. G. Dabbagh, D. P. Weliky, R. Tycko, *Macromolecules* **27**, 6138 (1994).
19. P. Robyr *et al.*, *Mol. Phys.* **84**, 995 (1995); M. Tomaselli *et al.*, *ibid.* **89**, 1663 (1996).
20. K. Schmidt-Rohr, *Macromolecules* **29**, 3975 (1996).
21. ———, *J. Magn. Reson.*, in press.
22. ———, W. Hu, N. Zumbulyadis, in preparation.
23. A. Bax, R. Freeman, S. P. Kempsell, *J. Am. Chem. Soc.* **102**, 4849 (1980); A. Bax, R. Freeman, T. Frankiell, M. H. Levitt, *J. Magn. Reson.* **43**, 478 (1981); R. R. Ernst, G. Bodenhausen, A. Wokaun, *Nuclear Magnetic Resonance in One and Two Dimensions* (Oxford Univ. Press, Oxford, 1987).
24. T. Nakai and C. A. McDowell, *Mol. Phys.* **79**, 965 (1993).
25. The 2D spectra were rotated by 90° from the traditional representation to simplify the comparison of the intensity patterns along the double-quantum dimension.
26. To make the PET sample amorphous, we quenched it from the clear melt into liquid nitrogen. The residual crystallinity was 5 ± 2% according to the following measurements. Wide-angle x-ray scattering (WAXS) showed only an amorphous halo (crystallinity < 8%). From the density $\rho = 1.34(4 \pm 2)$ g/cm^3 measured by flotation in a series of salt solutions, the crystallinity was estimated as 4.5 ± 1.5%, on the basis of amorphous and crystalline densities of $\rho_a = 1.33(6 \pm 2)$ g/cm^3 and $\rho_c = 1.5(1 \pm 2)$ g/cm^3, respectively. Thermal analysis (difference between crystallization and melting peak areas, with a heat of fusion Δh_f = 140 ± 20 J/g) yielded 8 ± 4% crystallinity. Cross-polarization–magic-angle spinning (CP-MAS) ^{13}C NMR showed no separate crystalline peak; selection of the long ^{13}C longitudinal relaxation time T_1 components yielded 3 ± 2.5% crystallinity.
27. The trans fraction of the amorphous phase was obtained as (18.5% − 5%)/0.95 = 14%.
28. The sample obtained by crystallizing the amorphous PET at 160°C for 2 hours had a crystallinity of 32 ± 4% by thermal analysis and 28 ± 4% by CP-MAS NMR. WAXS showed strong crystalline reflections.
29. In the semicrystalline sample, relatively fast relaxation of the spin-locked ^{1}H magnetization of the amorphous phase was observed. With a rotating-frame spin-lattice relaxation time $T_{1\rho}$ of ~4 ms, the signal from the amorphous regions observed in the ^{13}C spectrum was attenuated by 0.88 during the cross-polarization spin lock of 0.5 ms. Thus, the 47/53 (±6) trans/gauche ratio found in the spectrum had to be corrected slightly to 44/56 (±6).
30. G. Natta and P. Corradini, *Nuovo Cimento Suppl. Ser. X* **XV**, 13 (1960).
31. D. C. Clagett, in *Encyclopedia of Polymer Science & Engineering*, H. F. Mark *et al.*, Eds. (Wiley, New York, 1989), vol. 6, pp. 114–115; J. Y. Jadhav and S. W. Kantor, in *ibid.*, vol. 12, p. 219.
32. G. Strobl, *The Physics of Polymers* (Springer-Verlag, New York, 1996), pp. 169–172.
33. S. Roeber and H. G. Zachmann, *Polymer* **33**, 2061 (1992).
34. K. Schmidt-Rohr, M. Wilhelm, A. Johansson, H. W. Spiess, *Magn. Reson. Chem.* **31**, 352 (1993).
35. Generous financial support for K.S.-R. by a Beckman Young Investigator Award is gratefully acknowledged. Partial support was also provided by the NSF Materials Research Science and Engineering Center and by NSF grant DMR-9703916. K.S.-R. thanks M. Hong for stimulating discussions on data quantification.

23 October 1997; accepted 10 March 1998

Effect of Substrate Strain on Adsorption

M. Gsell, P. Jakob, D. Menzel*

Direct evidence for the effect of local strain at a surface on the bonding strength for adsorbates is presented. Scanning tunneling microscopy revealed that adsorbed oxygen atoms on Ru(0001) surfaces are located preferentially on top of nanometer-size protrusions above subsurface argon bubbles, where tensile strain prevails, and are depleted around their rim in regions of compression, relative to the flat surface. Such effects can be considered as the reverse of adsorbate-induced strain, and their direct local demonstration can be used to test theoretical predictions.

In recent years structure determinations of surfaces and adsorbate layers have become sufficiently exact to give detailed information about the structural changes at the surface compared with the bulk, and about the adsorption-induced shifts of substrate atoms (*1*). Even for surfaces without major rearrangement of the surface atoms (reconstruction), both lateral and normal (to the surface) shifts are found, which can vary considerably from one substrate surface atom to the next. Eventually the interatomic arrangements must join on to those of the undisturbed substrate lattice, so that considerable stress can exist in the near-surface region. Quite often these forces—which are, of course, the result of the changed bonding situation—lead to a major reconstruction, releasing some of the residual stress. Adsorption of gases causes complicated shifts of surface atoms (*1*, *2*), which should further modify these lateral and normal forces and interact with them.

On a more macroscopic scale, the developing stress can be made visible by tracing the deformation of thin crystals upon gas adsorption, either optically (*3*) or in a capacitive way (*4*). Adsorption introduces stress in the surface region of a crystal that can vary strongly on an atomic scale, causing displacements of substrate atoms from their original positions (strain), and the stress may also have an average component on a larger scale, allowing detection by macroscopic probes. On a mesoscopic scale the developing stress influences the morphology of bimetallic layers and local ordering (*5*).

Physik-Department E 20, Technische Universität München, D-85747 Garching, Germany.

*To whom correspondence should be addressed. E-mail: menzel@e20.physik.tu-muenchen.de

One would then expect that strain within the surface region of a crystal introduced by external influences should change its adsorptive properties. Theoretically, a dependence of the strength of adsorbate bonding on the surface lattice constant is expected, which should be quantifiable with large-scale, total-energy calculations. Obtaining direct experimental proof is not easy, however. For example, it is difficult to discern whether the changed adsorption strength at surface steps is primarily due to the (unquestionably existing) local strain or rather to additional electronic effects such as the electron redistribution under the strong electric field at a step. Applying an external force to bend the sample seems like the most promising way to study the intrinsic effect of strain on the adsorption properties of various gases. However, such macroscopically applied external forces will inevitably lead to the creation of numerous dislocations that form easily, especially for metals. On the other hand, external forces that are sufficiently weak not to be relaxed in this way will probably have only small effects, which would be difficult to discern. Another possibility, the formation of pseudomorphic substrate layers with crystal lattice constants different from the normal surfaces, has been used by Kampshoff *et al.* (*6*). The observed frequency shifts of the internal C-O stretch mode of adsorbed CO were interpreted by them in terms of lattice strain. However, effects other than the direct geometry change, especially structural defects in the bimetallic layers or dynamic frequency shifts, may also have affected their vibrational line positions.

We chose a way to create local strain fields and combined it with local imaging with the scanning tunneling microscope (STM). Local strain was produced on a

hexagonally close-packed Ru(0001) surface by means of subsurface gas bubbles induced by Ar^+ ion sputtering (kinetic energy = 1000 eV, current density = 5 $\mu A/cm^2$, sputter time = 20 min) followed by annealing at moderate temperatures (~1000 K). These procedures ensure that the sputter damage is healed completely, except for large and stable subsurface cavities filled with argon gas. Such cavities are well known from studies of plasma wall interactions and have been found to be stable against heat treatments (*7*); only annealing at temperatures above 1300 K leads to dissolution of Ar into the bulk and the disappearance of the protrusions on this surface. Recently, Varga *et al.* (*8*) demonstrated a quantum-size effect of the thin metal "lid" layer on such subsurface cavities for Al(111) using STM imaging. In their case the rather soft material easily develops dislocations at the rim of a subsurface cavity, which travel to the surface to create an island of monoatomic height. The pressure inside the cavity thereby gets released by volume enlargement, and strain built up in the surface region remains very limited or is relieved totally (*9*). For hard materials like ruthenium, such a strain elimination process would require much higher temperatures. The pressure increase by accumulation of dissolved Ar gas in the cavities therefore produces an upward bending of the uppermost layers.

In STM images, the Ru(0001) surface above such bubbles appeared as round domes of about 100 Å diameter and 3 Å maximum height. Because of the negligible compressibility of the Ru substrate, the size of the subsurface bubble is directly related to the size of the protrusion above the surface plane. We emphasize that the STM allows us to corroborate that no dislocations of the surface layers close to these protrusions existed. The lattice above the bubbles is therefore expanded, and the Ru surface layers are stretched laterally (producing tensile strain) and compressed vertically. The average lattice expansion due to the presence of a bubble can be simply determined by evaluation of the line integral across a typical protrusion (100 Å in diameter and 3 Å in height), which gives about 0.2% and which remains undetectable to the STM at present; the consequent average expansion of the substrate lattice amounts to only 0.005 Å per surface atom. However, the assumption of a uniform expansion would be true only if the lid above the bubble consisted of a single Ru layer, which would be stable.

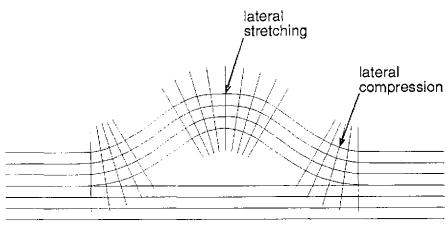

Fig. 1. Schematic cross-sectional view of an Ar subsurface bubble. The uppermost layer is stretched above the bubble and is compressed at the edges of the protrusions because of the opposite bending of the lid, which is composed of several metal layers.

Elasticity theory yields another, more important term that depends on the lid thickness and the curvature of the bending. With an educated guess for a realistic lid thickness of about 20 Å, an extra lattice expansion at its outer surface is expected that is on the order of 2 to 3% at the top of the dome (note that the exact thickness, which we do not know, is not important for our semiquantitative argument). Because of bending in the opposite direction of the surface layers at the edges of the protrusions, compression to approximately the same extent is expected there (Fig. 1). This model of nonuniform lattice strain is supported by our observations reported below. For these estimates we assumed negligible shear distortions within the substrate lattice unit cell, which would reduce the values given because of an extra lateral movement of substrate atoms to release stress. The general characteristics, expansion above and compression around the rim of the bubbles, however, remain valid. Besides the strain produced in this way, residual stress will exist in the layer, because there must be forces that balance those exerted by the Ar pressure in the bubble. These will lead to a variation of strain through the atomic layers below the surface, from the before-mentioned expansion of the top layer above the bubble—which is active in adsorption—through a neutral layer, to compression of the inner surface of the lid.

These local variations of surface strain can be probed by adsorption of a species that exerts additional stress on the lattice. Our observations with an STM show that strain introduced in the surface region of a close-packed, strongly refractory crystal on a mesoscopic scale (that is, extending over tens of substrate atomic spacings) strongly influences the strength of adsorption. Specifically, we found that in regions with lateral expansion and vertical compression the adsorption of oxygen atoms on Ru(0001) is stronger, whereas it is weaker in regions of lateral lattice dilatation. A qualitatively similar effect in terms of preferred adsorption areas is found for CO molecules. Both oxygen atoms and CO molecules are good probe particles because they are known to induce vertical as well as lateral shifts of Ru surface atoms (*10, 11*). Also, their mobility at room temperature ensures that the observed distributions are the result of local variations in adsorption energy, and kinetic limitations can be largely neglected. The surrounding flat terraces serve as a reference, because they provide a large number of alternative adsorption sites.

For mobile adsorbates on a heterogeneous surface the adsorption energy $E_A(x, y)$ is expected to be nonuniform with respect to lateral displacements (x, y) and can be expressed by a constant value E_{A0} plus a term $\Delta E_A(x, y)$ resulting from local strain fields. The expected occupation probabilities p of the various areas at a temperature T is given by $p(x, y) = p_0 \exp[-\Delta E_A(x, y)/kT]$, with p_0 denoting the respective value of a reference site with $\Delta E_A(x, y) = 0$, which is on the flat terrace, and k is the Boltzmann constant. Entropy factors are unimportant as long as the site geometry more or less stays the same and $\Delta E_A(x, y) \ll E_{A0}$, which is fulfilled in our case (where E_{A0} is on the order of a few electronvolts). Each adsorbate used in our study occupies only a single type of adsorption site. Because of the high mobility of the probe particles used (oxygen atoms and CO molecules), the different areas and their occupation probabilities are in thermal equilibrium with each other, and $p(x, y)$ can be related directly to local concentrations or coverages $\Theta(x, y) = \Theta_0 \exp[-\Delta E_A(x, y)/kT]$, with Θ_0 denoting the coverage on the flat terraces. The preferential occupation of energetically favored areas can then be directly monitored by using the atomic resolution of the STM. Methods such as detection of vibrational frequency shifts of probe molecules (*6*) extract information on the binding energy indirectly and only by the use of doubtful assumptions and therefore do not provide definitive answers.

A sequence of STM images for increasingly higher coverages of oxygen atoms on Ru(0001), obtained in ultrahigh vacuum at room temperature, is shown in Fig. 2 (*12*). Under these conditions oxygen molecules from the gas phase adsorb dissociatively with a sticking coefficient close to unity. In Fig. 2A, 0.02 monolayer (ML) of oxygen atoms was adsorbed, and the atoms were almost exclusively located on top of the protrusions produced by the Ar bubbles, indicating their strong preference for these laterally expanded lattice areas. In these areas, a (2×2) ordered oxygen superstructure is formed that represents a well-known arrangement for oxygen atoms on Ru(0001) at intermediate coverage ($\Theta_O \approx 0.25$ ML) (*10*); thus, there is a coverage increase by at least a factor 10. When the average Θ_O is increased to ~0.2 ML, which approaches completion of the O(2×2) overlayer, an

interesting nonuniform distribution of oxygen atoms is produced, with a depletion zone around the protrusions (Fig. 2B). The tops of the bubble lids remain unchanged because they have already been covered by a (2×2) layer at much lower Θ_O. On the terraces, large islands of O(2×2) with jagged boundaries were observed; fast-moving single oxygen atoms were found to commute between neighboring islands, ensuring thermal equilibrium conditions (*13*). The depletion zone with a radial extent of about 20 Å from the edge of the bubble toward the flat terrace remains clearly defined. The oxygen density in this area is reduced to one-fifth of that on the regular terraces, which means that the oxygen binding energy is less favorable by about 40 meV. Of course, the extent of depletion is subject to statistical fluctuations and it varies with the dimensions of the numerous protrusions examined, so that the given number for ΔE_A is an approximate value.

At an oxygen coverage of 0.25 ML, these depletion zones disappear to yield a homogeneous O(2×2) layer (*14*). With further increased O_2 exposure an O(2×1) overlayer (*11*) forms, with the oxygen atoms arranged in rows along the substrate lattice directions (Fig. 2C). Three domains, rotated by 120° with respect to each other, are possible. The top of the protrusion area is again populated first as soon as Θ_O exceeds 0.25 ML. Similarly to the low-coverage layer (Fig. 2A), the oxygen atoms are preferentially adsorbed in the laterally expanded lattice on the bubble top. Unlike the O(2×2) structure, the rowlike O(2×1) structure has an anisotropic stress tensor. Stress release can thereby be optimized by selecting the most favorable orientation among the three domains. As is apparent in Fig. 2C, the compressive surface strain in the boundary zone of the bubbles leads to a tangential orientation of the O(2×1) rows. This is in agreement with the concept of repulsive interactions between the oxygen atoms within the dense O(2×1) rows. These domains extend into the flat terraces by about 5 to 10 rows, counterbalancing the larger O(2×1) domains that form on the flat surface surrounding the protrusions; the resulting domain boundaries are seen to be continuously moving. This appreciable local mobility means that, as in the case of the depletion zone (Fig. 2B), the observed domain boundaries correspond to an equilibrium situation. If one goes beyond the $\Theta_O = 0.5$ ML coverage, corresponding to a complete O(2×1) layer, toward the 3O(2×2) layer (*15*), or toward the completely filled O(1×1) on Ru(0001) layer (*14*), again additional adsorption first happens on the bubble top, easily seen by formation of the respective ordered oxygen overlayer structure.

These observations suggest that the expansive stress associated with oxygen adsorption and formation of the various superstructures leads to the preferred occupation of areas where the substrate lattice is stretched, whereas those parts of the surface experiencing compressive lateral strain are the least favorable zones and therefore will be covered last. In addition, the anisotropic stress tensor associated with the O(2×1) overlayer leads to a preferred tangential orientation of the oxygen rows along the rim of the Ar-bubble lid tops.

Preliminary results on the effect of the molecular adsorbate CO could indicate that these influences of adsorbate-induced stress and strain on adsorption energy and the consequent selection of different areas may also be possible in the opposite direction. As shown in Fig. 2D, adsorbing CO seems to avoid the bubble top. At a coverage close to 1/3 ML, the well-known ($\sqrt{3} \times \sqrt{3}$)R30° structure (*16*) is formed on the terraces, whereas the bubble top seems to remain essentially free of CO, with some molecules moving rapidly across the protrusion (again indicated by short horizontal dashes). However, these observations could also be explained by the formation of a very dense CO layer on the bubble top, because very low corrugation in STM and high adsorbate mobility are also found for these conditions. That there is a change of adsorption energy here as well is undebatable, even though the sign is not yet certain.

As mentioned in the introduction, the effects of strain could in principle be calculated with large-scale density functional calculations, although we are not aware of any publications. Still, the application of these calculation methods to such effects are by no means trivial [see, for instance, (*17*) for a controversy about possible changes of the normal distance at a surface, which is a related question] and may be complicated by residual stress that must exist in situations like ours, which is associated with the layer-dependent variation of strain in the bubble lid. Results by Nørskov *et al.* (*18*) on the dependence of adsorption energy on substrate lattice parameter, that is, the surface strain, indicate that the sign of the effects observed here for oxygen can be understood by such calculations. For CO the same behavior would be expected as for oxygen from these calculations; as discussed, the experimental evidence in this case is not yet clear-cut. If further work should prove that there is indeed a contradiction there, this could be connected with the neglect of the layer-dependent strain mentioned above.

Increased theoretical and experimental efforts are therefore required to understand these effects in detail. These should be worthwhile in view of the fundamental and practical importance of these interactions, because practical active surfaces of catalysts and the like may contain such influences, and the multilayer semiconductor systems used extensively in modern devices are in many cases strained and stressed.

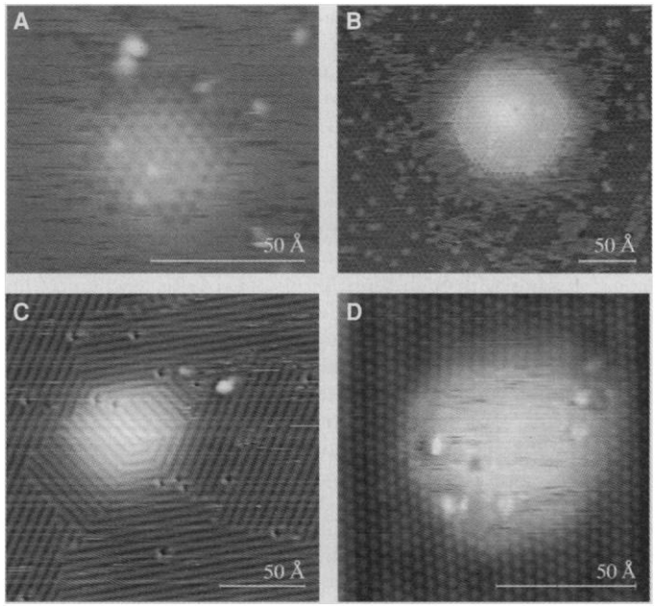

Fig. 2. STM images demonstrating the locally selective adsorption on and around Ar bubbles as a result of local dilatations and compressions. (**A**) At low overall coverage of oxygen atoms (about 0.02 ML), the oxygen atoms preferentially cover the stretched areas of the protrusion tops in a (2×2) arrangement of local coverage of 0.25 ML. (**B**) At overall coverage of 0.2 ML, the surface is largely covered by the O(2×2) superstructure, except for a depleted ring in the compression zone at the rim of the protrusion. (**C**) At an overall oxygen coverage of 0.5 ML, the O(2×1) rows are arranged on and tangentially around the bubble to adapt most favorably to the anisotropic strain field at the rim of the bubble. (**D**) CO coverage close to 1/3 ML. The flat and compressed areas are covered by a well-ordered ($\sqrt{3} \times \sqrt{3}$)R30° superstructure of CO molecules, whereas the bubble top appears to be essentially uncovered. However, this could also be due to formation of a much denser CO layer in this region.

REFERENCES AND NOTES

1. P. R. Watson, M. A. Van Hove, K. Herrmann, Eds., *Atlas of Surface Structures* (*J. Phys. Chem.* Ref. Data, Monogr. No. 5, American Institute of Physics, New York, 1995).
2. D. Menzel, *Surf. Rev. Lett.* **4**, 1283 (1997).
3. R. E. Martinez, W. A. Augustyniak, J. A. Golovchenko, *Phys. Rev. Lett.* **64**, 1035 (1990); A. J. Schell-Sorokin and R. M.Tromp, *ibid.*, p. 1039.
4. V. Buck, *Z. Phys. B* **33**, 349 (1979); D. Sander and H. Ibach, *Phys. Rev. B* **43**, 4263 (1991).
5. R. Schuster, H. Röder, K. Bromann, H. Brune, K. Kern, *Phys. Rev. B* **54**, 13476 (1996); G. Ritz, M. Schmid, A. Biedermann, P. Varga, *ibid.* **53**, 16019 (1996).
6. E. Kampshoff, E. Hahn, K. Kern, *Phys. Rev. Lett.* **73**, 704 (1994).
7. H. Trinkaus, *Radiat. Eff.* **78**, 189 (1983).
8. M. Schmid, W. Hebenstreit, P. Varga, *Phys. Rev. Lett.* **76**, 2298 (1996).
9. H. Ullmayer, *Radiat. Eff.* **78**, 1 (1983).
10. M. Lindroos, H. Pfnür, G. Held, D. Menzel, *Surf. Sci.* **222**, 451 (1989).
11. H. Pfnür, G. Held, M. Lindroos, D. Menzel, *ibid.* **220**, 43 (1989).
12. No Fourier or other filtering was applied, but the contrast was adjusted to make the structures in the very different regions visible simultaneously.
13. At low-oxygen coverages $\Theta_O < 0.1$ ML, oxygen atoms have high mobility at room temperature, and their average residence time per lattice site (0.05 s) is smaller than that required for their complete imaging. However, because of the line-by-line scanning of the STM image, fast-moving oxygen atoms can be easily recognized by the horizontal dashes that correspond to incomplete images of them.
14. M. Gsell, P. Jakob, D. Menzel, data not shown.
15. K. L. Kostov *et al.*, *Surf. Sci. Lett.* **394**, L138 (1997).
16. G. Michalk, W. Moritz, H. Pfnür, D. Menzel, *Surf. Sci.* **129**, 92 (1983).
17. D. Menzel, *ibid.* **318**, 437 (1994), and references given therein.
18. M. Mavrikakis, B. Hammer, J. K. Nørskov, private communication.

19. Supported by the Deutsche Forschungsgemeinschaft through Sonderforschungsbereich 338.

7 January 1998; accepted 10 March 1998

Micromechanical "Trampoline" Magnetometers for Use in Large Pulsed Magnetic Fields

V. Aksyuk,* F. F. Balakirev, G. S. Boebinger, P. L. Gammel, R. C. Haddon,† D. J. Bishop

A silicon micromechanical magnetometer was constructed and successfully used in 60-tesla pulsed magnetic fields of less than 100-millisecond duration. The device is small, inexpensive to fabricate, and easy to use. It features a fast mechanical response (up to 50,000 hertz) and extremely high sensitivity yet is relatively robust against electrical and mechanical noise. Quantum oscillations in the magnetization of a 1-microgram sample of an organic superconductor, κ-[bis(ethylenedithio)tetrathiafulvalene]$_2$Cu(NCS)$_2$, have been observed with this device.

Pulsed magnetic fields exceeding 30 T have recently become more readily available to small laboratory-based research groups. The discharge of a large bank of capacitors through a compact solenoid composed of several hundred turns of wire with a very high tensile strength generates a rapid high-field magnetic pulse. The pulse duration (typically a few tens of milliseconds) and repetition rate (three pulses per hour) are both limited by the substantial heating of the solenoid during the pulse.

Making accurate measurements in pulsed magnets can be a challenge because of the short duration of the pulses and the considerable electrical and acoustical noise in the sample environment. Furthermore, although magnets of this design can survive as many as 1400 60-T pulses, stress on the solenoid may on occasion lead to explosive failure during a pulse. Thus, experimental probes need to be reasonably reproducible and relatively inexpensive.

We report here on a micromachined silicon "trampoline" device that allows magnetization to be measured for a wide range of solids with high sensitivities over time scales consistent with the decay times of a typical pulsed magnet. The magnetometer operates as a Faraday balance: When placed in a magnetic field gradient, a sample experiences a force proportional to the magnetization of the sample multiplied by the magnitude of the field gradient. If the sample is attached to a spring, measuring the sample displacement is equivalent to measuring the force exerted by the magnetic field gradient. A scanning electron microscope image (Fig. 1A) of the magnetometer shows the square micromachined polysilicon plate, typically 300 to 500 μm on a side, that is freely suspended by four soft springs, one at each corner. One of the four springs is shown in Fig. 1B. When mounted, the sample is affixed to the center of the polysilicon plate and both are free to move vertically together by an amount, δz, in response to the force, $\mathbf{F} = \nabla(\mathbf{M}\cdot\mathbf{B})$, where $\mathbf{M}$ is the magnetization of the sample and $\mathbf{B}$ is the magnetic field (*1*). In practice, this displacement is detected by measuring the capacitance (from 0.3 to 1.1 pF) between the mobile polysilicon plate and a fixed polysilicon plate of the same size (not visible in Fig. 1), located directly under the mobile plate.

The two plates are separated by a ~2-μm gap created by the etching of an SiO_2 sacrificial layer, a process that was facilitated by an array of small etch holes 20 μm apart in the mobile plate (Fig. 1B). An array of small posts (60 μm apart) protrudes from the bottom of the mobile plate to prevent the two plates from touching and adhering to one another. The capacitance measurement can be made on a very short time scale (~30 μs), with a resolution as high as 1 part in 10^4, by the application of a 1-V, 100-kHz excitation to the leads. For the device to have a high sensitivity to the magnetization of the sample, the springs must be soft enough (~1 N m^{-1}) to allow a measurable displacement in response to very small forces. Silicon surface micromachining allows a wide latitude in designing the mechanical properties of the magnetometer plates and springs without reducing the mechanical robustness of the suspended polysilicon plate (*2*).

The magnetometer is best suited to small samples, which tend to be more homogeneous than large samples and more immune to unwanted heating (which can result from eddy currents induced in the sample by the pulsed magnetic field). Its small size results in high mechanical resonant frequencies (typically >10 kHz, which can be tuned by altering the design of the springs), which yields sufficiently fast mechanical response times. Although the pulsed magnet generates mechanical vibrations during the pulse, this mechanical noise occurs at much lower frequencies (<100 Hz) and thus couples very little to the mechanical resonances of the magnetometer.

We confirmed the desired operation of the magnetometer by measuring the mechanical response of the structure to applied electric fields. To determine the mechanical resonance frequencies of the magnetometer, we measured the displacement between the magnetometer plates with a lock-in amplifier while the frequency of a 1-mV ac excitation voltage was swept from nearly dc up through the various resonant frequencies of the device. The lowest resonant frequency, f_{res}, of the particular device used in the experiments described below to de-

V. Aksyuk, P. L. Gammel, R. C. Haddon, D. J. Bishop, Bell Laboratories, Lucent Technologies, Murray Hill, NJ 07974, USA.

F. F. Balakirev and G. S. Boebinger, Bell Laboratories, Lucent Technologies, Murray Hill, NJ 07974, USA, and Los Alamos National Laboratory, MS E536, Los Alamos, NM 87545, USA.

*To whom correspondence should be addressed. E-mail: aksyuk@physics.bell-labs.com

†Present address: Departments of Chemistry and Physics, University of Kentucky, Lexington, KY 40506, USA.